Near Surface Geophysics

EAGE
EUROPEAN
ASSOCIATION OF
GEOSCIENTISTS &
ENGINEERS

Cost-effective in-mine seismic experiments to image platinum deposits and associated geological structures at Maseve platinum mine, South Africa

Moyagabo K. Rapetsoa[1], Musa S.D. Manzi[1*], Michael Westgate[1], Mpofana Sihoyiya[1], Ian James[2], Emmanuel Onyebueke[1], Phumlani Kubeka[3], Raymond J. Durrheim[1] and Thabang Kgarume[4]

[1] *School of Geosciences, University of the Witwatersrand, Johannesburg, South Africa,* [2] *Terraspect Geophysics, Perth, Australia,* [3] *Royal Bafokeng Platinum, The Pivot, Fourways, South Africa, and* [4] *Council for Scientific and Industrial Research, Pretoria, South Africa*

ABSTRACT

The detection of mineral deposits and their related geological structures is of great importance to the mining industry as structures (such as dykes and faults) can affect the safety, cost and efficiency of mining. With the goal of testing cost-effective seismic methods for mineral exploration and mining, active and passive seismic experiments were conducted at Maseve platinum mine in the Bushveld Complex (South Africa) in 2020. The experiments involved surface-passive (using 5 Hz wireless nodes; single vertical component) and in-mine active reflection seismic surveys (using 4.5 Hz land streamer and 5 kg sledgehammer) to image geological structures and delineate economic platinum-group elements bearing Merensky and Upper Group-2 chromitite layers (known as reefs). This paper presents only the results from the in-mine active seismic experiments. The in-mine seismic surveys consisted of seven 2D reflection seismic profiles in the development tunnels, which were located ~550 m below ground surface and a few tens of metres above known mineralizations: the Upper Group-2 and Merensky Reef. The data were carefully processed to enhance the reflections and suppress noise generated by mine infrastructure (e.g., equipment and ventilation). We successfully imaged the Merensky Reef and Upper Group-2 orebodies approximately 55 m and 124 m below the tunnel floor, respectively, and delineated faults and dykes that crosscut them. Furthermore, the seismic data reveal relatively strong amplitude and faulted reflections below the Upper Group-2 that may represent deeper chromitite-enriched orebodies. However, the economic value of these horizons can only be confirmed through drilling. The processed seismic data were combined with borehole data, synthetic modelling and geological models to constrain the interpretation. This study encourages the use of in-mine seismics for future mineral exploration, mine development and planning.
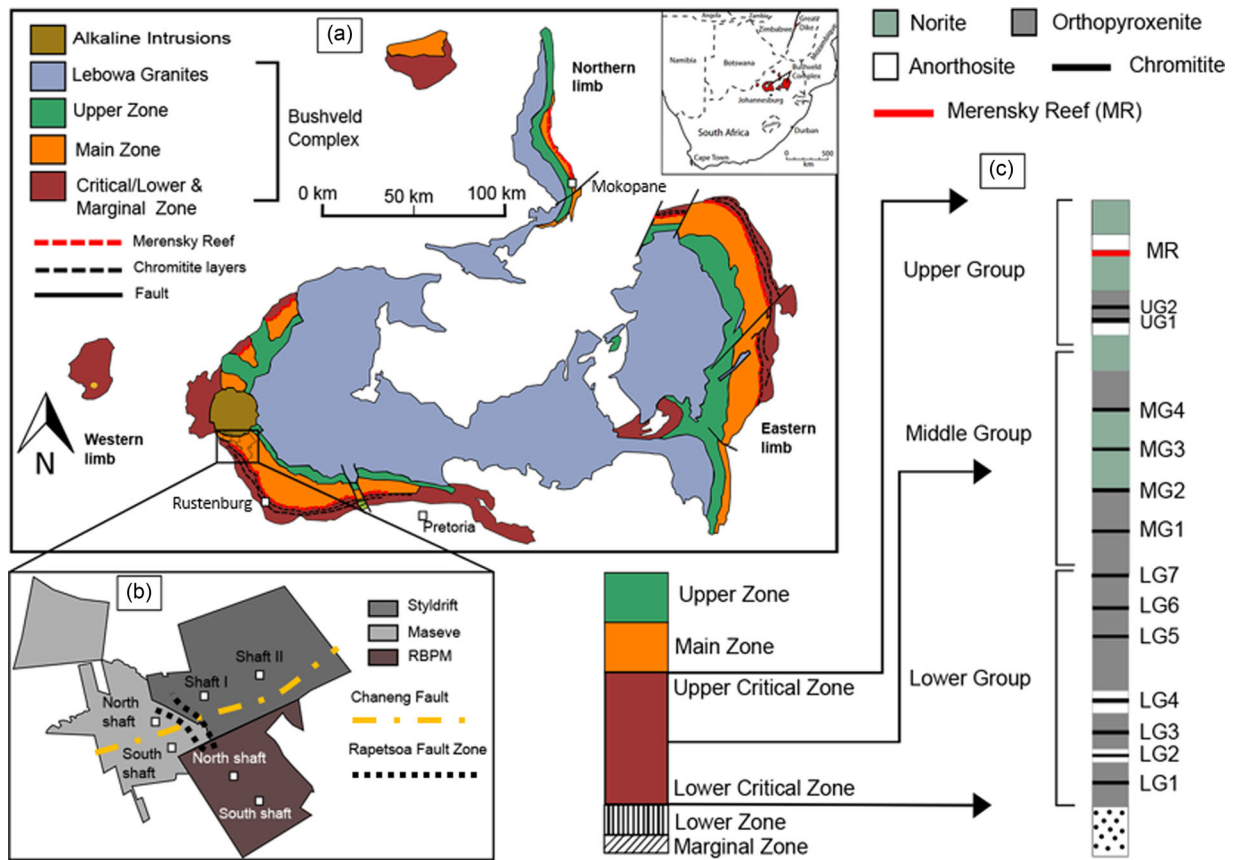
Key words: Seismic, Imaging, Tunnel, Integration, Near-surface.

INTRODUCTION

The Bushveld Complex, located in the northern parts of South Africa, is the world's largest layered igneous intrusion with an estimated area of 64,000 km^2. It hosts the world's largest

*E-mail: musa.manzi@wits.ac.za

Figure 1 (a) Geological map of the Bushveld Complex (modified from Cawthorn, 2015) showing the location of the Maseve mine site. (b) Map of the Maseve mine showing the location of the study area at the north shaft and the surrounding mines that are used for seismic surveys. The orange dashed lines show the ENE–WSW trending Chaneng fault, while the black dotted lines show the NE–NW trending fault (here termed Rapetsoa Fault Zone (RFZ)). (c) Stratigraphic column of the critical zone showing the chromitite layers and Merensky Reef (MR). RBPM: Royal Bafokeng Platinum Mine; UG: Upper Group; MG: Middle Group; LG: Lower Group.

reserves of platinum-group elements (PGEs) and accounts for almost 80% of all platinum that is mined worldwide (Chistyakova *et al.*, 2019).

The PGE deposits occur at various locations around the perimeter of the Bushveld Complex. The Maseve mine is located ∼ 38 km NW of Rustenburg and ∼ 10 km south of the Pilanesberg Alkaline Intrusive Complex in the North West Province, South Africa. The mine is situated on the western limb of the Bushveld Complex, next to the Styldrift and Wesizwe mines (Figs 1 and 2). The mine was placed under care and maintenance in 2017 due to economic reasons and is currently used to test new mining technologies, making it an ideal site for field research.

Underground mining operations in the Bushveld Complex occur between 0.5 km and 2.0 km below surface. Geological structures (e.g., faults, dykes, potholes, and Iron Rich Ultramafic Pegmatites (IRUPs)) are encountered more frequently

as mining depth increases (Eales and Cawthorn, 1996; Sehoole *et al.*, 2020). These geological structures not only delay development and production, but also threaten the safety of mineworkers by increasing the risk of fall of ground that can result in injuries and fatalities (Guo and Luo, 2014). Furthermore, faults and dykes may act as conduits for flammable gases and groundwater to the mining levels, which may lead to disasters in the mines. These structures can also be re-activated during mining activities and cause rock bursts. The heightened risks compromise the fundamental principles governing South African mining; i.e., safety and optimized ore extraction. These problems highlight the growing need for these geological structures to be identified ahead of mining.

The reflection seismic method is one of the most important geophysical methods because of its ability to detect both large and small-scale subsurface features (Malehmir *et al.*, 2012). In South Africa, the reflection seismic method is
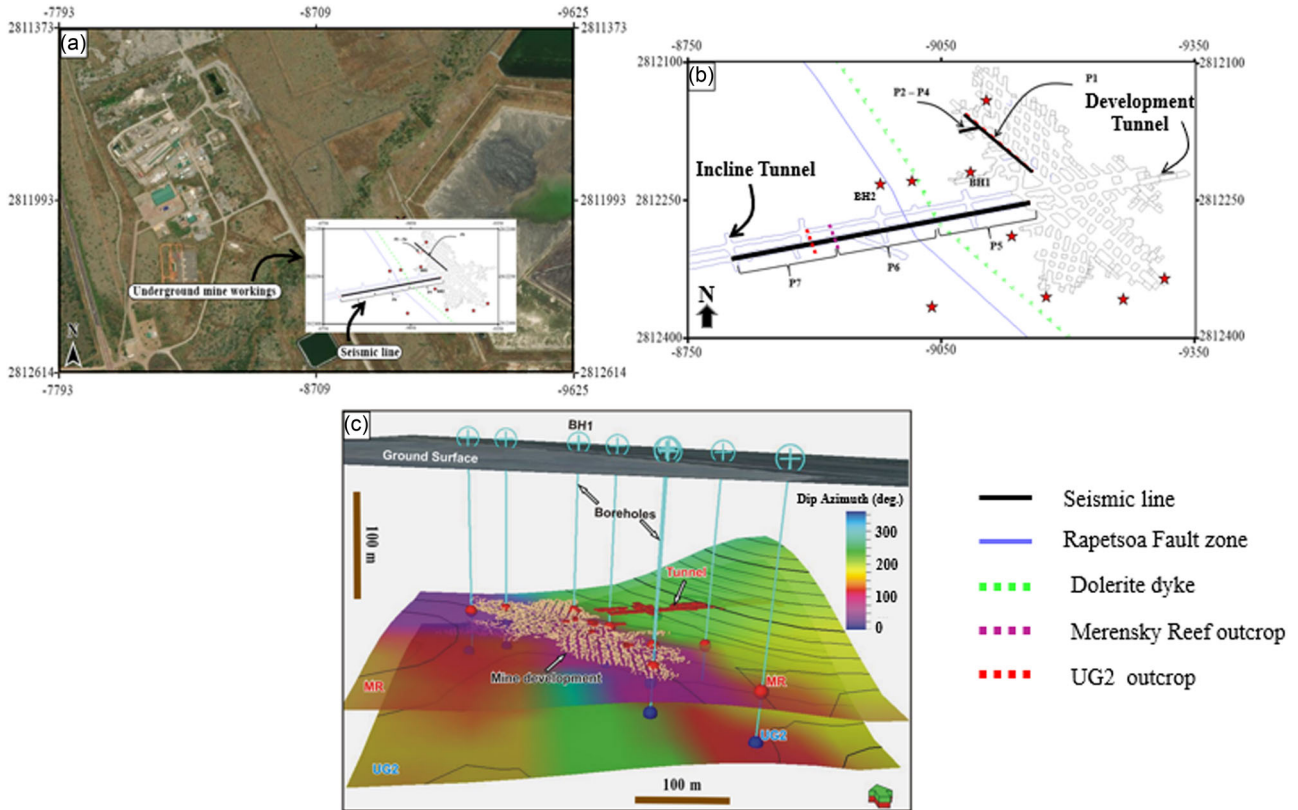
Figure 2 (a) Map view of the Maseve mine surface workings and underground working indicating the seismic profile (black) collected. (b) Underground mine plans, showing the location of the seismic profiles (black) and geological structures such as fault (blue) and dolerite dyke (green) for in-mine seismic experiments. (c) A schematic 3D geological model of the study area, showing the Merensky Reef (MR), Upper Group 2 reef (UG2) and the incline tunnel (red) (the green arrow is pointing to the south). The position of the seismic line is indicated along the incline tunnel. BH1: borehole 1; BH2: borehole 2; P1: profile 1, P2–P 4: profile 2 to profile 4; P5: profile 5; P6: profile 6; P7: profile 7.

mainly used for exploration, mine design, and planning, due to its ability to delineate complex geological features (Stevenson and Durrheim, 1997; Manzi *et al.*, 2012; Manzi *et al.*, 2019).

Active surface reflection seismic surveys have been conducted since the 1980s in South Africa to address challenges related to deep and near-surface mineral exploration, with the goal of reducing drilling and exploration costs, maximizing mine safety and increasing the possibility of finding new prospects and the life of mine. In the 1990s, exploration and mining companies started conducting high-resolution surface 2D and 3D reflection seismic surveys in the Bushveld Complex to map economic platinum-bearing horizons (known as reefs) and other subsurface features (faults, dykes, folds and potholes). The 3D reflection seismic surveys were particularly designed to map major faults, dykes, potholes (slump structures), and IRUPs. However, the surface seismic surveys were unable to accurately map and provide the geometry of smaller geological structures ahead of mining tunnels (Trickett *et al.*,

2004). In the early 2000s, trials were conducted to investigate technologies that can delineate subtle structures with a throw of $\sim$ 2 m (Stevenson *et al.*, 2003). The trials mainly involved borehole seismic techniques (e.g., cross-well reflection seismics, seismic tomography and vertical seismic profiling), which produced resolutions of 1 to 3 m; however, these techniques exhibited low resolutions in noisy mining environments (Stevenson *et al.*, 2003; Manzi *et al.*, 2012).

As an alternative solution, and despite suffering from noise produced by mine operations such as blasting, ventilation and drilling, in-mine seismics has proven useful in improving the imaging resolution of the mineral deposits and geological structures (Brodic *et al.*, 2017, 2021; Donoso *et al.*, 2021). The application of in-mine seismic techniques has grown worldwide; however, the techniques are not yet well established in deep South African mines.

In this study, we conducted 2D in-mine seismic surveys at Maseve platinum mine in the Bushveld Complex (South

Africa) to characterize geological structures using different seismic data acquisition techniques. The seismic experiments were conducted in an area covered by ground-penetrating radar (GPR) and electrical resistivity tomography (ERT) surveys for integrated interpretation purposes. Integration of geophysical and geological data has played a key role in mapping; the deep geological structures and obtaining information on/ahead of the tunnel face. GPR and ERT are commonly used to map tunnel roofs and sidewalls, the information of which is in turn utilized to assess and mitigate fall of grounds due to unstable hangingwalls (Kgarume *et al.*, 2019). However, in this paper, we present only the results from the in-mine seismic trials.

The extent to which in-mine seismic techniques can image structures depends on multiple factors: acoustic impedance contrast; the geometry and structural characteristics of the target; host rock properties; survey design (receiver and source position); and the mine noise level along the tunnel. To better design in-mine seismic surveys and conduct high-resolution seismic surveys, noise levels need to be assessed and appropriate sources and receivers need to be used. Furthermore, accurate velocity models for the rock mass around the tunnel need to be determined for numerical modelling, seismic processing, interpretation and time-to-depth conversion (Malehmir *et al.*, 2013; Manzi *et al.*, 2017).

STUDY AREA AND GEOLOGICAL BACKGROUND

The emplacement of the Bushveld Complex has been the subject of academic debate, and its geology has been documented by several authors (Eales and Cawthorn, 1996; Buchanan and Reimold, 1998; Kinnaird, 2005; Hunt *et al.*, 2018). The intrusive rocks of the Bushveld Complex were emplaced at ~2.06 Ga into the intra-cratonic sedimentary sequence of the Transvaal Supergroup (Cawthorn and Webb, 2001). The Bushveld Complex is known for its remarkable size, covering an area of about 64 000 km^2. The complex (Fig. 1) is composed of four major limbs, with only the eastern, western and northern limbs outcropping. The southern limb is visible only from gravity data and has been confirmed by drilling. Over the years, several authors have debated about the limbs being connected (Webb *et al.*, 2004; Kinnaird, 2005). The successive injections of magma resulted in the geology of the area being divided into three plutonic suites: the Rashoop Granophyre Suite; the mafic to ultramafic Rustenburg Layered Suite (RLS); and the Lebowa Granite Suite (Eales and Cawthorn, 1996; Hunt *et al.*, 2018). Based on mineralogical variation, the RLS

is further divided into the (from bottom to top): Marginal; Lower; Critical; Main; and Upper Zone (Kinnaird, 2005).

The Critical Zone is about 900–1500 m thick and has been divided into the Lower Critical Zone (LCZ) and the Upper Critical Zone (UCZ) based on the appearance of cumulus plagioclase. The LCZ is characterized by pyroxenites, Lower Group chromitite layers (LG) and Middle Group chromitite layers (MG1 and MG2), whereas the UCZ is characterized by the Merensky Reef (MR; a package of platinum-bearing chromitite-feldspathic orthopyroxenite), Upper Group chromitites (UG1 and UG2), Middle Group chromitites (MG3 and MG4), pyroxenites, norites and anorthosites (Kinnaird, 2005; Seabrook, 2005). The upper limit of the UCZ is marked by the Bastard Reef (referred to as cyclic/rhythmic unit) (Cawthorn, 2015). The MR and the UG2 chromitite are the two major economic horizons for PGE deposits. The thickness of the MR ranges from 0.5 m to 2.0 m, with an average thickness of 1.0 m. The UG2 chromitite layer contains the largest PGE resources on Earth, with a thickness ranging between 0.5 m and 1.0 m. The Middle Group (MG) is made up of four major and minor chromitite layers with a thickness of 0.01-0.05m, whereas the LG consists of seven chromitite layers, with the thickest being 0.8–1.2 m (Lee, 1996; Nex *et al.*, 1998; Kinnaird, 2005). The MR and the UG2 are mined at depths greater than 500 m below surface at the Maseve mine, with the UG2 occurring between 15 m and 400 m below the MR in the Bushveld complex (Manzi *et al.*, 2020; Sehoole *et al.*, 2020).

The Bushveld Complex is crosscut by multiple dykes of different ages and compositions, with diabase and dolerite dykes being dominant in the area. A few dykes at the Maseve mine have been confirmed through drilling and underground mapping. Knowledge of the dykes is important as they reduce the ore reserve and may present mining difficulties. The dykes in the Bushveld Complex are often associated with fault zones (Ledwaba *et al.*, 2012; Scheiber-Enslin and Manzi, 2018). Furthermore, the Bushveld Complex is affected by slump structures (locally known as 'potholes') and IRUPs that result in challenges to mining operations. The Bushveld Complex is generally faulted, and the regional structural interpretation suggests that the ENE–WSW trending Chaneng Fault Zone (Fig. 1b) is the most dominant structure in the Maseve area (Basson, 2019). To the south of the Pilanesburg complex, a dense conjugate network of faults and fractures trending NE and NW is displayed on the high-resolution aeromagnetic images (Scheiber-Enslin and Manzi, 2018; Basson, 2019). These geological features have been confirmed through drilling at the Maseve mine and incorporated in the geological model

Table 1 Physical property measurements of Bushveld Complex rocks. Velocity and density of feldspathic and pegmatoidal pyroxenite are adapted from Manzi *et al.* (2020).

Rock type	ν (m/s)	ρ (kg/m^3)
Merensky Reef (orthopyroxenite)	5950	2744
UG2 (chromitite)	6118	4392
Anorthosite (pegmatoidal)	5530	2947
Anorthosite (weathered)	3088	2851
Norite	5667	2951
Feldspathic pyroxenite	5400	3000
Pegmatoidal pyroxenite	5900	2700

ν = P-wave velocity ρ = density.

(Fig. 2). Most of the faults strike north to northwest and dip at an average of about 70° to 80° (Scheiber-Enslin and Manzi, 2018).

PHYSICAL PROPERTY MEASUREMENTS

Physical property measurements were collected following the procedure described by Nkosi *et al.* (2017). The main objective was to investigate the potential source of seismic reflectivity of the mineralization (Merensky Reef (MR) and Upper Group-2 (UG2)) with respect to their host rocks. The ultrasonic velocity (P-wave) measurements were conducted using a UK1401 SURFER ultrasonic tester, operating at frequencies of 50 kHz. Throughout the seismic P-wave velocity measurements, the repetition frequency of the instrument was kept constant between 2 Hz and 4 Hz, depending on the size of the sample. Five P-wave velocity measurements were taken on each sample and an average was taken as the final velocity value (Table 1). Although the ideal conditions for measuring these samples are at elevated pressures ($\sim$ 20–60 MPa) to mimic the in situ environment, our measurements were conducted at atmospheric temperature and pressure. The bulk density measurements were conducted using the water immersion method (based on Archimedes' principle) (Nkosi *et al.*, 2017). Another factor that affects acoustic impedance is porosity; however, in this study, we did not conduct porosity measurements as the rock samples are from a crystalline environment and have comparable porosity (Malehmir *et al.*, 2013; Nkosi *et al.*, 2017).
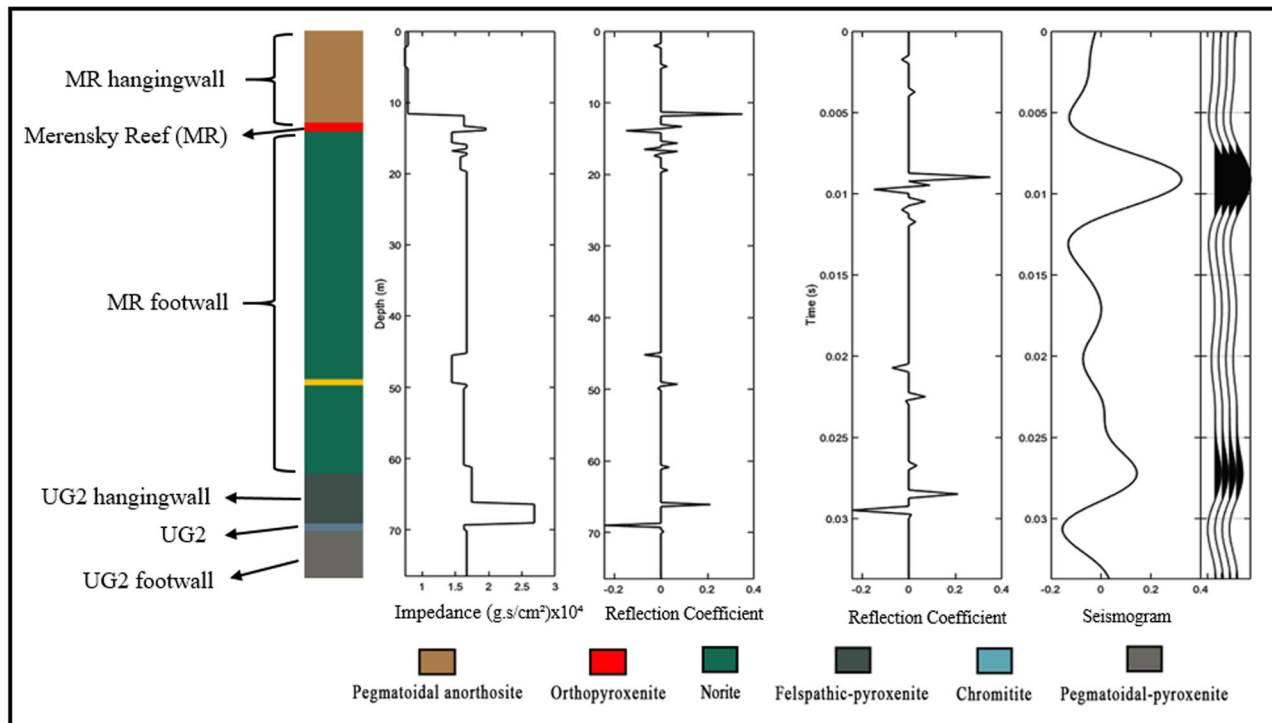
Synthetic seismogram

This section presents results of the physical property measurements (bulk density and seismic velocities) of rocks in the Bushveld Complex that make up the hanging wall and foot-

wall of the MR and UG2. Previous studies have reported seismic velocities and densities of rocks in the Bushveld Complex (Campbell, 2011; Manzi *et al.*, 2017); therefore this study reports in detail the individual density and velocity measurements of the hanging wall and footwall in the study area. We used the information to design the seismic experiments to investigate 'near-surface' geological structures, i.e. within 150 m of the mine tunnel in which the survey was conducted. Table 1 summarizes the ultrasonic velocities and density measurements of the MR, MR hanging wall, MR footwall and UG2. While the velocity and density of feldspathic and pegmatoidal pyroxenite are from Manzi *et al.* (2019), the densities and velocities of the rocks are within a narrow range, except for the chromitite sample that is much denser than the host rocks and the water-saturated top layer of norite that has a lower velocity. The average P-wave velocity measurements of the core samples range from 3088 m/s to 6118 m/s and the average density measurements range from 2700 kg/m^3 to 4392 kg/m^3. To compute the synthetic seismograms, we used the measured densities, velocities and depths from borehole 1 (BH1; see Figs 2 and 3). The borehole has a total depth of 577.5 m from the Earth's surface and intersected the MR and UG2 at 515.14 m and 570.94 m, respectively. We used a Ricker wavelet with a dominant frequency of 130 Hz and a sampling rate of 0.25 ms to compute the seismograms for the lower 75 m of the borehole, which covered the ore zones beneath the tunnel (Fig. 3). The acoustic impedance contrast between the hanging wall and footwall of the MR suggests that the interface is associated with a strong reflection, which can be used as a proxy for MR mineralization. The UG2 has a higher acoustic impedance contrast with the host rocks; hence, a noticeable reflection at the interface (Fig. 3), which is in agreement with studies conducted by Scheiber-Enslin and Manzi (2018) and Manzi *et al.* (2020).

2D acoustic modelling and seismic reflectivity

The geology of the Maseve mine is detailed in the mine's resource estimation report (Muller and Visser, 2010). The Bushveld Complex has been well studied (Nex *et al.*, 1998; Webb *et al.*, 2004; Kinnaird, 2005; Cawthorn, 2015), and the geological structures in certain areas make it an ideal place to conduct numerical modelling to investigate the seismic response of mineralizations and other geological structures. However, the Bushveld Complex rocks (anorthosite, norite and pyroxenite) have similar physical properties (mainly seismic velocities). Acoustic impedance contrast in the Bushveld Complex is mainly controlled by noticeable differences in

Figure 3 Stratigraphic column derived from borehole 1 (BH1) of the Maseve mine. Reflection coefficients were derived from the acoustic impedance, and synthetic seismograms were generated using the reflection coefficient and a Ricker wavelet (130 Hz). Generated reflections are associated with the two major reefs (Merensky Reef and UG2). The impedance contrast of the Merensky Reef (MR) and its hangingwall is high due to the water-saturated hangingwall and low velocities of the anorthosite rocks in the hangingwall. The acoustic impedance of the Upper Group 2 (UG2) and the surrounding rock is typically high compared to that of the MR (see Manzi et al., 2020).

the densities of the rocks, which in turn provides a strong reflective interface between the mineralization and the host rocks. The MR has a slightly higher seismic velocity than the host rock, while the UG2 has a higher density compared to the host rocks (Table 1). The focus of the study is to image the near-tunnel-floor mineralization and geological structures; therefore, the complex geology of the area is not presented in detail. The thickness and depth of the targeted mineralizations were obtained from the available surface boreholes in the study area (Figs 2 and 3). The MR (∼ 1–2 m thick) and UG2 (∼ 1–2 m thick) were intersected by surface borehole (BH1) at depths of 515 and 571 m, respectively. These horizons are faulted and folded (asymmetrical synclinal fold with a NW–SE trending fold plane), resulting in the MR and the UG2 outcropping on the west-south-west (WSW) side of the seismic line (Fig. 2b). The acquired seismic profiles (mainly P5 and P6) transverse a major dolerite dyke and the fault zone (here termed Rapetsoa Fault Zone (RFZ)) that crosscut the MR and UG2 (Fig. 2). Seismic modelling only considers the rocks beneath the tunnel. The rock between the

tunnel and the Earth's surface is considered to be free space. The elevation of the inclined tunnel is used as the datum for reflection seismic processing. Therefore, the complex characteristics of the full 3D wavefield are not analysed in this paper.

The modelling was conducted using Tesseral Pro software. Figure 4 shows the geological model built (Ahmadi et al., 2016; Singh et al., 2020) from borehole data and mine information (Fig. 2). The 2D acoustic finite-difference modelling was conducted to assist with the planning of the in-mine seismic surveys, to investigate the source of seismic reflectivity in the data and to constrain seismic interpretation. The structures identified from the mine plan (Fig. 2b) were used to build a geological model (Fig. 4) of the rock mass beneath the incline tunnel. The finite-difference model was 360 m (horizontal extent) × 140 m (depth), with a grid cell of 1 m in both vertical and horizontal directions. A synthetic 2D seismic survey was designed to generate 2D synthetic shot gathers using acoustic modelling (Fig. 5a) of the first few hundreds of metres for two shot examples (Fig. 5a, d: first and centre shot). The main objective of numerical modelling was to simulate the
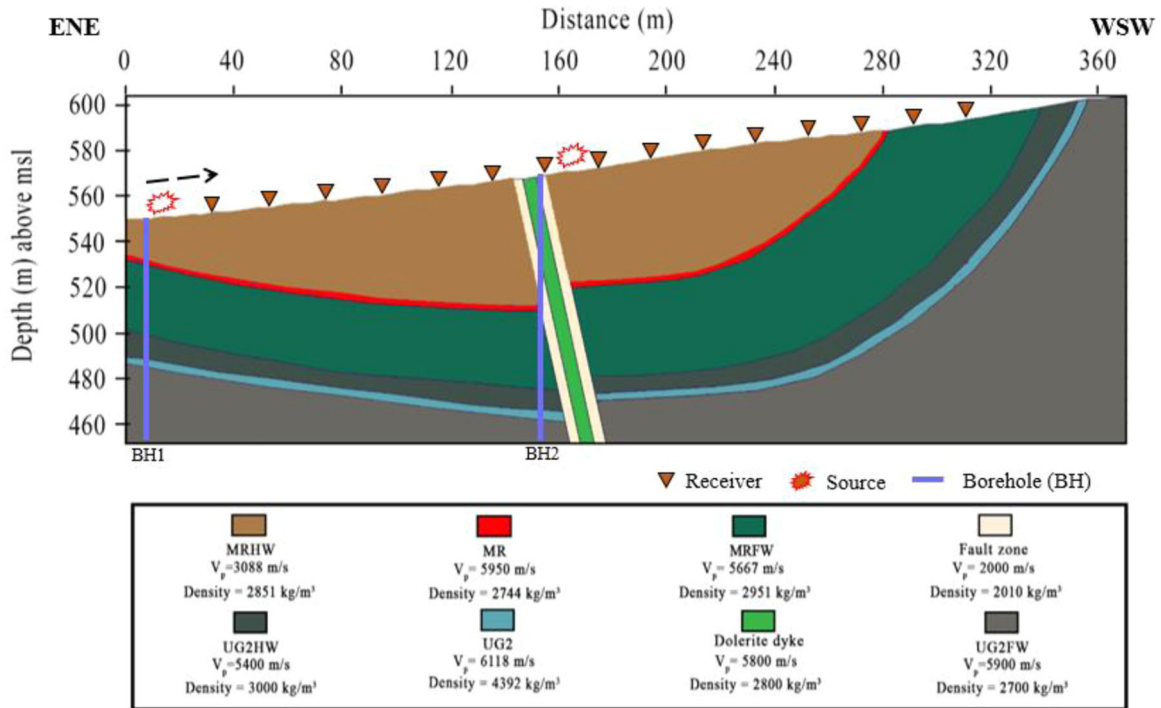
Figure 4 Geological/finite-difference model at the Maseve mine. The model shows the two-target mineralizations (MR and UG2) and geological structures (fault and dyke). The velocity and density of the rocks are noted. The receiver (brown) and shot (red) positions are shown, together with the acquisition direction (ENE–WSW) over an incline. The boreholes used for the model as shown (purple) MRHW: Merensky Reef hangingwall (Weathered Anorthosite; MR: Merensky Reef (orthopyroxenite); MRFW: Merensky footwall (norite); UG2HW: Upper Group 2 hangingwall (feldspathic-pyroxenite); UG2: Upper Group 2 (chromitite); UG2FW: Upper Group 2 footwall (pegmatoidal pyroxenite); msl: mean sea level; BH: Borehole.

seismic response of the targets (MR and UG2) and geological structures (faults and dykes). The synthetic data were generated using the acquisition parameters very close to the ones used for real seismic surveys, except that the model used a single profile (360 m long), while the real survey data had three merged profiles (115 m long). The synthetic seismic modelling had a maximum two-way travel time of 500 ms. A Ricker wavelet of 130 Hz was used for modelling, with a sampling rate of 0.25 ms. The measured average velocities and densities in Table 1 were used in the model. The shot gathers of the synthetic data (Fig. 5a, d) were then compared with those of the acquired data (Fig. 5b, e). The comparison between the synthetic and real data is discussed later.

SEISMIC DATA ACQUISITION

Prior to the seismic surveys, a preparatory mine site visit was made for a few days to check the tunnel conditions and decide on the location of shots and receivers. Information from the ground-penetrating radar and electrical resistivity tomog-

raphy surveys conducted in the tunnel a few weeks prior assisted in designing our surveys to better delineate the targets (depth and lateral extent of the deposits, as well as geological structures).

In November 2020, seven 2D in-mine seismic profiles were acquired with a total length of about 0.6 km over known orebodies (Fig. 2a, b). The final set-up included: one profile in the development tunnel (P1); two around Michelle's pillar (P2 and P4); one profile in a crosscut (P3); and three profiles (P5, P6 and P7) in the incline tunnel (Fig. 2b). The three incline tunnel profiles, namely P5 (115 m long), P6 (115 m long) and P7 (115 m long), were collected in segments that are collinear to each other, orientated in an east-north-east (ENE) to west-south-west (WSW) direction (Fig. 2b). P5, P6 and P7 profiles are the focus of this paper and were designed to cover the area along the incline tunnel. P1 was collected perpendicular to P5–P7, with the goal of imaging the folded Merensky Reef (MR) and Upper Group-2 (UG2) located at about 20–70 m depths below the incline tunnel (Fig. 2b). P2 and P4 were experimental lines collected around the pillar of interest. The idea being to test the response of the 4.5 Hz geophone (1C)
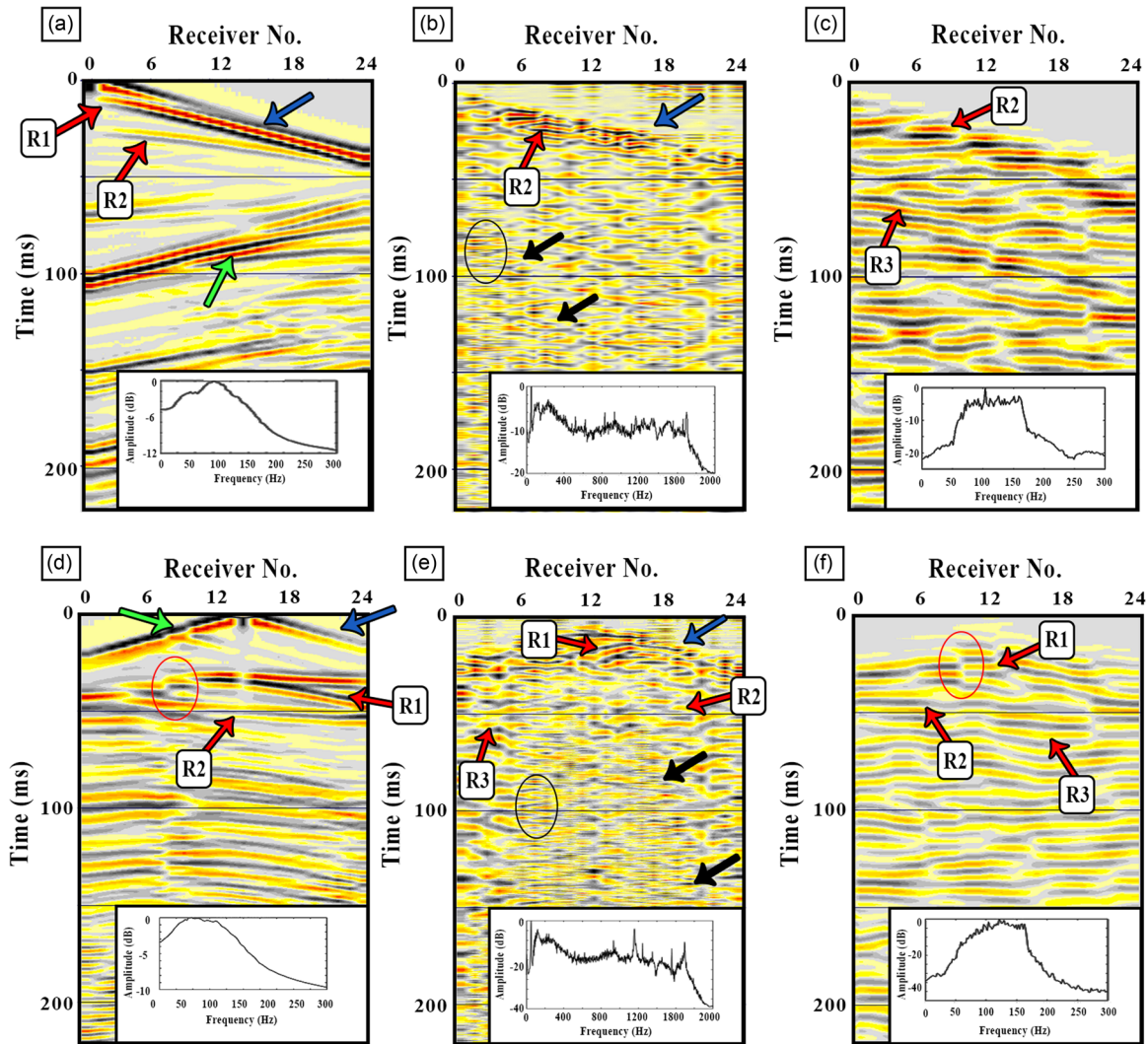
Figure 5 Shot gathers examples from P5 (see Fig. 2b) first shot and middle shot, with their frequency spectra. Shot gathers highlight clear reflections marked by red arrows. (a and d) Synthetic shot gathers modelled from the geological model; (b and d) raw shot gathers; (c and d) processed shot gathers. (a) Clear reflection (R1: 10 ms, R2: 27 ms) from the UG2 and diffractions (green) due to the dyke and fault zone. (b) Raw shot gathers with reflections overshadowed by high frequencies (black circle), airwaves are indicated by black arrows and first breaks are indicated by blue arrows. The frequency spectrum has frequency ranges of 0–1800 Hz as a result of the sampling rate of 0.25 ms. (c) The processed shot gathers showing clear reflections, with one of the reflections not easily identified on the synthetic gather and the raw shot gather. (d) R1 (29 ms) originates from the Merensky Reef and R2 (45 ms) originates from the UG2. The modelled dyke and fault zone disturb R2 (red circle). (e) R1 at 20 ms, R2 at 45 ms and R3 at 55 m are observed on the raw shot gather. (f) The three reflections observed (R1, R2 and R3) are enhanced after pre-stack filtering.

attached to the land streamer along the pillar; the shots were generated horizontally along the pillar using a 5 kg sledge-hammer. P2 was conducted at the base of the pillar, whereas P4 had receivers supported on the sidewall. P3 was collected with planted cabled sensors (1C; 4.5 Hz and 14.0 Hz), while the other 5 segments were collected using a 4.5 Hz seismic land streamer. The profiles collected with the land streamer had a receiver spacing of 5 m, providing a total spread of 115 m.

A day was spent testing different sources (24 kg acceler-ated weight drop (AWD) and a 5 kg sledgehammer), and one-component sensors (cabled 100 Hz horizontal, 14.0 Hz ver-tical and 4.5 Hz land streamer). We also drilled holes along the tunnel floor to plant the cabled geophones and increase the coupling; however, this process proved time consuming as it took about half a day to plant geophones along one profile. This encouraged the use of the land streamer as re-

Table 2 In-mine seismic acquisition parameters at the Maseve mine

Line	P1	P2	P3	P4	P5	P6	P7
Number of receivers	24	24	24	15	24	24	24
Profile length	115 m	26 m	26 m	28 m	115 m	115 m	115 m
Direction	SW-NE	On Pillar	SE-NW	On Pillar	SE-NW	SE-NW	SE-NW
Recording length	500 ms	300 ms	150 ms	150 ms	500 ms	500 ms	500 ms
Sample interval				0.25 ms			
Vertical stacks				4			
Source spacing	5 m	2 m	5 m	5 m	5 m	5 m	5 m
Source type				5 kg Sledgehammer			
Receiver spacing	5 m	2 m	1 m	2 m	5 m	5 m	5m
Geophone frequency	4.5 Hz	4.5 Hz	4.5&14 Hz	4.5 Hz	4.5 Hz	4.5 Hz	4.5 Hz

ceivers in all seismic profiles because it was quick and provided better coupling with the tunnel surface. Shots were generated with both sources to check the signal-to-noise ratio (S/N) of the data and decide on the most suitable seismic source for the surveys. Although the 24 kg AWD provided a better signal, it was not safe to use due to the conditions of the tunnel sidewall and hanging wall (e.g., loose fragments of the hanging wall). A 5 kg sledgehammer was used as a seismic source instead, with a shot spacing of 5 m. To improve S/N, four shot records were vertically stacked at every shot position. A range of sampling rate parameters were also tested to ensure that guided waves and other mine-related noise, for example, were not contaminating the records. Following the analysis of the shot gathers at various sampling rates, a sampling rate of 0.25 ms was chosen as it provided better results with respect to the limitations of the resonant and spurious frequencies of sensors used in the survey. The survey parameters are detailed in Table 2. One of the advantages of the sledgehammer is its light weight and low cost when compared to other seismic sources. The mine is also prone to flammable gases (e.g., methane), so we carefully ensured that the hammer's impact on a base plate did not generate any sparks that could lead to explosions inside the tunnel.

In addition to the seismic surveys conducted along mine tunnels, five active seismic profiles were collected on the surface, simultaneously with passive seismic surveys using three broadband seismometers and remote acquisition units. The surface experiments were an attempt to test the feasibility of conducting tunnel-surface experiments. In this paper, only the results obtained from active in-mine seismic profiles (P5–P7) are presented.

SEISMIC DATA PROCESSING

Figure 5 shows the comparisons between the synthetic (Fig. 5a, d), raw (Fig. 5b, e) and processed (Fig. 5c, f) shot records. The raw seismic data exhibit a high signal-to-noise ratio (Fig. 5b). However, a few traces exhibit some noise due to airwaves (Fig. 5b, e: black arrows) or poor coupling of geophones on the muddy areas along the tunnel. Table 3 provides the workflow followed in the processing of the data, subdivided into pre-conditioning and processing steps. The main aim of the processing workflow was to preserve primary reflections and remove source-generated and ambient noise (e.g., water pipes, moving vehicles and blasting from neighbouring mines) to improve data quality.

The first step was to fix the coordinates and merge the seismic profiles (P5–P7) before processing because the headers had receiver and shot positions as coordinates. Coordinates from the mine pegs were used to determine the shot and receiver locations, using linear and spline interpolation functions. The second step was to fix the geometry. From the coordinates created, a shell-processing-support file was set up for the geometry. The geometry was then merged with the seismic data. For the seismic profile, we assigned common depth points with a spacing of 2.5 m, followed by removing noisy traces, mainly caused by poor ground coupling.

The data are of fair quality, with clear P-wave first breaks in the raw shot gathers (indicated by blue arrows in Fig. 5b, e). Some reflections (R1 and R2) observed in the raw shot gathers (red arrows in Fig. 5b, e) matched reflections in the synthetic shot gathers (Fig. 5a, d). R1 is interpreted to originate from Merensky Reef (MR) and is not clearly defined in the first shot synthetic gather (Fig. 5a); it is masked by first breaks as

Table 3 Processing steps applied to the Maseve mine, South Africa, in-mine seismic dataset.

Pre-conditioning		Parameters
Create coordinates	✓	Linear and spline interpolation
Create SPS files	✓	Merge the coordinates of P5–P7
Processing		**Parameters**
Data input + reformat	✓	From SEGD to SEGY
Geometry assignment + CDP bin	✓	Sources and receivers assigned to each trace + CDP size 2.5 m
Trace editing	✓	Kill noisy traces
First break picking	✓	Automatic, manual picking
Floating datum statics correction	✓	Fixed datum elevation: 602 m (below surface). Replacement velocity: 4000 m/s
Refraction static correction	✓	Two-layer model based on the first break picking. Root-mean-square error 1.45–2 ms
Trace muting	✓	Top mute using first breaks
Bandpass filtering	✓	50–60–160–170 Hz
Automatic gain control	✓	Window: 50 ms
Balance	✓	500 ms
F–k filtering	✓	Surgical muting, dip = 1.2 m/s per trace
Velocity analysis	✓	Constant velocity stack
NMO corrections	✓	5500–6500 m/s, stretch mute: 70%
Residual statics	✓	Repeat NMO corrections twice
DMO	✓	Kirchhoff common offset
Stack	✓	Normal
Bandpass filtering	✓	80–90–150–160 Hz
Post-stack time migration	✓	2D Kirchhoff
Time-to-depth conversion	✓	Constant velocity: 5500 m/s

the reflecting MR is close to the tunnel floor on the east of the model (Fig. 4). R2, on the other hand, is well defined at 25 ms with a weak reflection compared to R1. Possible reflected refractions from the fault (RFZ) zone and dyke are also observed in the synthetic data (Fig. 5a, d: green arrows). R1 (30 ms) and R2 (45 ms) are clearly observed on the centre synthetic shot gather and the raw shot gather. An additional reflection (R3: 55 ms) is also observed on the raw shot gather.

As one of the most important steps in the pre-stack data processing stage, the P-wave first breaks were picked using an automatic method (envelope threshold) combined with manual picking. The picks were used to compute the refraction statics. A total of 1778 picks were used over 72 receivers and 76 shots across the three profiles. The picks were inverted for the two-layer-based refraction model, with four iterations and an RMS error of 1.45–2.00 ms. Figure 6 shows a refraction tomogram (Fig. 6a) and a ray path model with low ray coverages (white arrows in Fig. 6b). The low ray coverage is as a result of merging the three segments into one profile (Fig. 6b). The refraction tomogram (Fig. 6a) was produced to aid with the interpretation of the data for about 20−50 m depth below the incline tunnel. The maximum elevation along the profile is 602 m (above mean sea level) and was chosen as a matching datum elevation together with a replacement velocity of

4000 m/s for floating datum statics. The next step was to apply refraction, residual (using only short wavelength component) and elevation statics correction to enhance the continuity of the reflections and improve the quality of the final seismic section.

Figure 5(b and c) shows the raw shot gathers and a processed shot gather (trace editing, refraction static, bandpass filter and top mute), respectively. The raw data are contaminated by some noise that could be related to ambient sources (i.e., ventilation and water pumps; Fig. 5b). The frequency of the acquired data ranges from 50 Hz to 1800 Hz. The higher frequencies (> 250 Hz) are most likely related to spurious frequencies of the 4.5 Hz geophones used. A bandpass filter (50–170 Hz) was applied to constrain the data within the source energy frequencies. The amplitudes of the first breaks (Fig. 5b, e) are high, affecting the near-surface reflections. To remedy this, we applied top mutes on the first breaks with care in order to not mute some shallow reflections. The processing steps applied illuminated reflections (R2 and R3) in the shot records (Fig. 5f). Although the above-mentioned processing steps enhanced some of the reflections, some noise (probably related to airwaves) were still present in some shot records (Fig. 5b, e: black arrows) and overshadowed the reflections (e.g., R2). To eliminate these, an *f–k* filter was applied to the data. The *f–k*
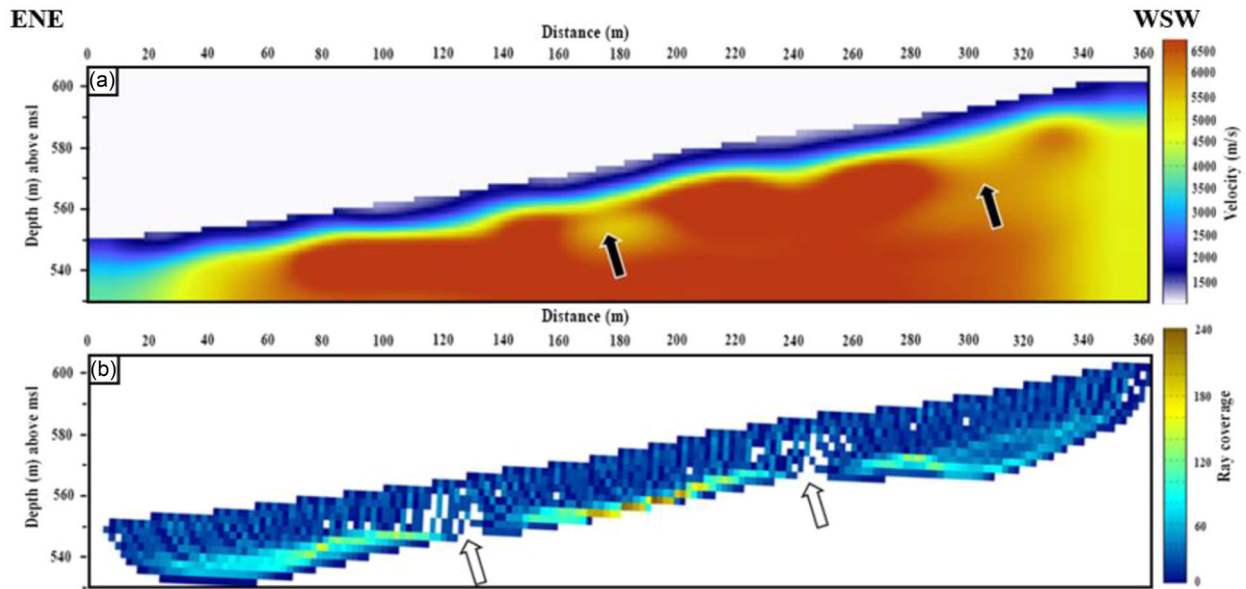
Figure 6 (a) Near-surface P-wave velocity model showing the upper 70 m of the incline tunnel. Black arrows indicated lower velocity zones, which are associated with geological structures intercepted alone the line. (b) Ray path model showing ray coverage of the velocity model. The white arrows indicate an area of low fold and where the three segments were merged. msl: mean sea level.

filter targeted events with velocities below 4100 m/s, in order to enhance the targeted events that have apparent velocities between 5700 m/s and 6400 m/s.

Velocity analysis was conducted using a series of constant velocity stacks generated to select the velocity that showed highest coherency of the reflections. Prior to stacking, Normal Moveout (NMO) corrections were applied to account for the hyperbolic curvature of the reflections and stacked using the NMO velocities of ~5500 m/s. We calculated and applied residual statics using the updated NMO-corrected gathers, resulting in continuous reflections on the stacked sections. Dip moveout was applied to stack the dipping reflections simultaneously. A second bandpass filter (80–160 Hz) was applied to remove low frequencies that were still present in the data. Figure 7 shows the final unmigrated time (Fig. 7a) and depth-converted (Fig. 7b) stacked sections, respectively. A Kirchhoff migration algorithm was applied using a constant velocity of 5500 m/s, which was decided based on the P-wave velocity distribution on the data and published velocities (Manzi *et al.*, 2020). Finally, following a series of tests on velocity fields that provided the best migrated sections, 5500 m/s was used for time-to-depth conversion. Together with mine-modelled structures and surface boreholes, the final depth-converted seismic section was imported into the 3D visualization software package for final geological interpretation and comparison with other geological datasets.

RESULTS AND INTERPRETATION

Seismic processing and interpretation were mainly constrained to the top 100 ms (approximately 275 m depth below the tunnel floor) because the main targets (Merensky Reef (MR) and Upper Group-2 (UG2)) for future mining and exploration at Maseve mine fall within this window (Figs 5–9). The first step was to make a comparison of the synthetic, raw and processed shot gathers (Fig. 5). Clear first arrivals (blue arrows) are seen in the 2D acoustic finite-difference modelled shot record, raw short record and processed shot record (Fig. 5). The airwaves (indicated by black arrows) observed in the raw shot gather (Fig. 5b, e) has been attenuated (Fig. 5c, f) by applying filters (mainly *f–k*) and dip moveout, resulting in a dataset with an improved signal-to-noise ratio. The main reflections observed in the seismic data interpreted to have originated from the mineralizations are MR (R1) at 20 ms, UG2 (R2) at 45 ms and a possibly unknown mineralization (R3) at 55 ms (Fig. 5e, f). MR is shallower toward the ENE on the model. Therefore, the strong reflection (R1) originates from MR and is coupled with the first breaks, while the weak reflection (R2) originates from the UG2. R3 is not modelled in the synthetic data (Figs 4 and 5a) as it was not known, but is visible in Fig. 5(b, e). R3 is interpreted to originate from the UG1, which is a chromitite mineralization that is well known in other mines within the Bushveld Complex. UG1 is, however, not intersected by drilling at the Maseve mine as the drilling
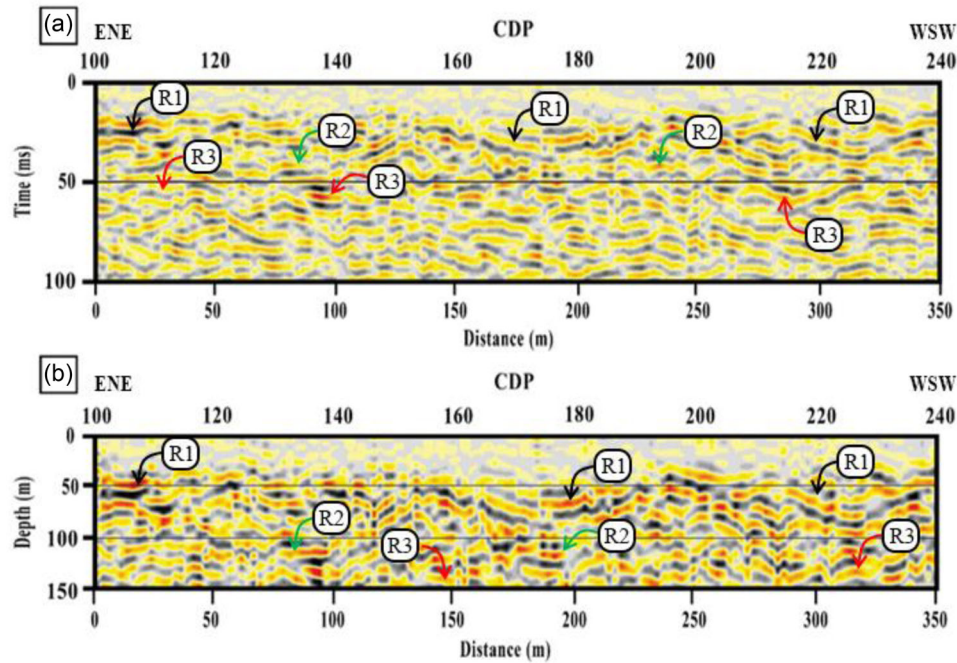
Figure 7 Comparison of unmigrated (time) stack (a) and depth stack (b) sections of incline tunnel profile (P5-P7). Clear reflections (shown with black arrows) are more prominent at the centre of the sections. Time stack section shows strong reflections at 20 ms (black), which correspond to 55 m depth in (b), while the dipping reflections (green arrows) at about 45 ms correspond to 124 m on the depth section. Third reflection (red arrows) is shown at 55 ms and is expected at a depth of 151 m.

only targeted MR and UG2 (Fig. 2c). Our interpretation of this seismic reflection (and others observed in the data) is not conclusive as these events could be associated with complicated wavefield characteristics caused by side tunnels connected to the main exploration tunnel, fracture systems, the rock mass around the tunnel and mine infrastructure (or developments). In addition, there is no borehole information to further constrain our seismic interpretation below the UG2 horizon.

P-wave velocities obtained from the first break tomograms show a good definition of two zones in our area: fractured top layer ($\sim$ 10 m thick) exhibiting velocities between 1000 m/s and 4000 m/s and the hard rock exhibiting variable thicknesses (10–40 m) with velocities between 4000 m/s and 6500 m/s. These velocities show a good match with the known velocities from (norite and pyroxenite; Manzi *et al.*, 2020) and borehole stratigraphy and complement P-wave reflectivity observed on the final stacked sections (Figs 7 and 8). Based on the refraction tomograms, existing borehole, geological models (Fig. 2) and tunnel observations (i.e. outcropping MR and UG2 $\sim$ 110 m and $\sim$180 m WSW of the centre of the merged profile, respectively), the stratigraphy generally dips at $\sim$ 10° towards WSW and dips 60° ENE due to folding and faulting (Fig. 4).

The unmigrated time (Fig. 7a) and depth-converted (Fig. 7b) stacked seismic sections suggest that the reflections are well delineated in our study. The strong reflectivity observed at 20 ms (black arrows) on the time stack section corresponds to 55 m depth on the depth stack section. The reflections (Fig. 7a, b: marked with arrows) are more prominent at the centre of the seismic section. The shallow reflection occurring at about 55 m is attributed to the MR, as discussed previously. The far ends of each seismic profile (P5–P7) show reflections that may be related to processing artifacts, while the middle section (CDP: 160-180; 200-230) shows more coherent reflections due to the high fold-of-coverage (Fig. 8a). Overlaying the borehole log and 1D synthetic data onto the depth-converted migrated section (Fig. 8b) confirms that the strong reflections (R1) at about 55 m depth can be attributed to the MR, while the reflection at $\sim$124 m (R2) is associated with the UG2. The reflector (R2) dips towards west-south-west and loses coherency at CDP 130. The area is structurally complex as interpreted in Fig. 9. MR and UG2 are affected by folding (e.g., a synclinal structure is observed between CDP 160 and 200) and crosscut by dykes (dotted green and red lines) and faults (indicated by pink lines) different orientations (Fig. 9). In addition to faults and dykes, the seismic section
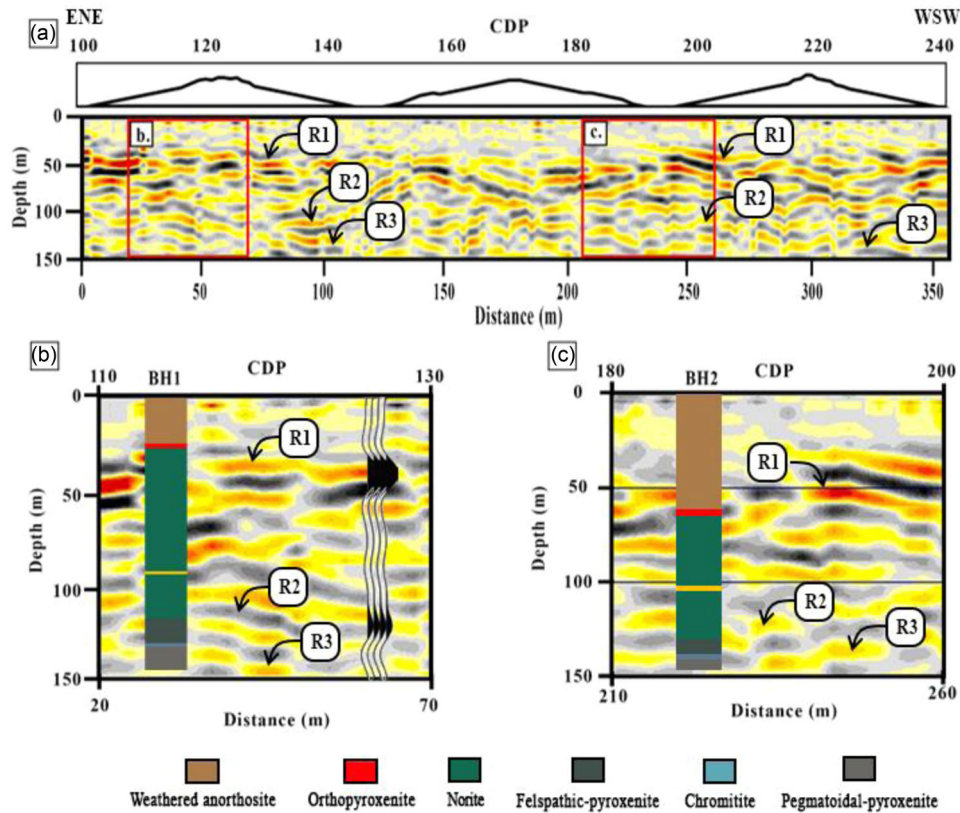
Figure 8 Depth-converted migrated seismic section; red outline shows the focus area where boreholes 1 and 2 are overlaid. (a) Migrated stack section of profiles P5–P7 with (b) Borehole 1 and synthetic seismogram overlaid (BH1; see Fig. 2). Reflection R1 correlates with the Merensky Reef (MR) and reflection R2 correlates with UG2. The arrows mark the identified reflector detailed in the text. (c) Borehole 2 correlated with the migrated section.

exhibits a vertical low-seismic amplitude and chaotic feature along the MR and UG2 horizons, which is interpreted to be associated with the IRUP (Fig. 9; IRUP: dotted brown). Similar to faults and dykes, this feature appears to disrupt both the MR and UG2 (Figs 8 and 9), and it occurs in the vicinity of the fault zone. In particular, the seismic sections show the delineation of F4 that coincides with the RFZ interpreted in the mine geological model and described by several authors. Identification of these structures by the seismic data is important as this information can be used to enhance the existing geological model.

DISCUSSION

To better understand the quality of the data and interpret geological structures, it is important to first address the seismic resolution limit of the data. The quality of the acquired data is dependent on many factors such as the impedance contrast between the target and the host rock, the geometry (e.g., shape) and thickness of the target, survey design, instruments used, tunnel conditions and noise level. The seismic resolution limit is controlled by the dominant wavelength (λ) in the data, seismic velocity of the targets and the dominant frequency of the data. Theoretically, the top and bottom of geological features cannot be resolved if its thickness is less than a quarter of the dominant seismic wavelength (i.e., Rayleigh criteria of the vertical resolution limit). However, smaller features down to $\lambda/32$ can still be detected, although the detection will depend on the diffractions, not solely on the seismic amplitude (Manzi *et al.*, 2014; Malehmir *et al.*, 2018).

The dominant seismic frequency of the reflected signal at the Merensky Reef (MR), for example, is $\sim$ 130 Hz. By taking into account the stacking velocity ($\sim$ 5500 m/s) used in our processing workflow, the dominant seismic wavelength (λ) is $\sim$ 42 m. This gives us the vertical resolution limit of $\sim$ 10.5 m, which is the minimum thickness needed to resolve the top and bottom of a layer. However, the MR ($\sim$1–2 m thick) and Upper Group-2 (UG2) (1–2 m) are too thin to be resolved. Hence,
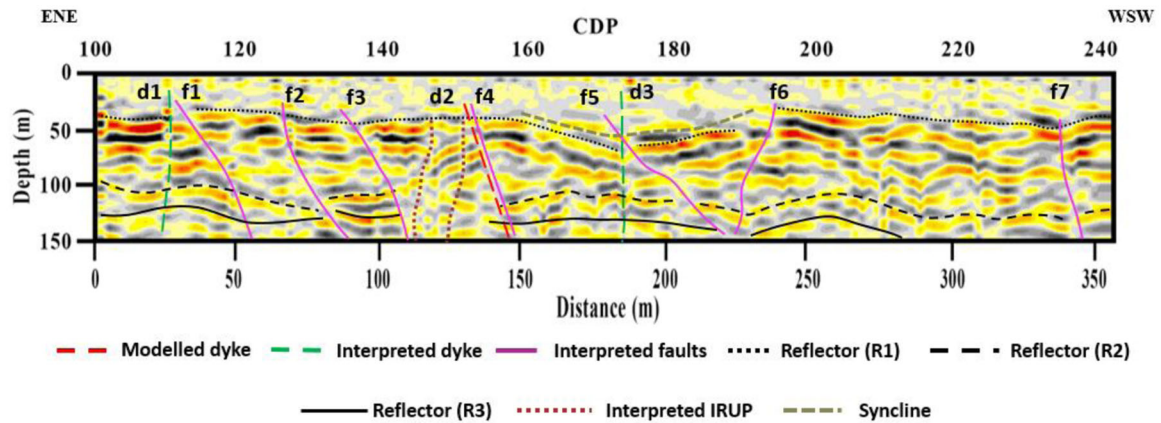
Figure 9 Interpreted migrated section (in depth) of seismic profiles P5-P7. The Merensky Reef (MR) reflector is marked with dotted lines (R1), and UG2 is marked with a dashed line (R2). Third reflection marked with a solid line is linked with the UG1. The reflections are not continuous at areas of the low fold. The reflector is displaced by a combination of normal and reverse faults (purple solid lines). Dashed lines (green) are the interpreted dykes, while the red dashed line is the position of the dyke and fault zone (see Fig. 4). R1 is bent (grey dashed line) between CDP 160 and 190, which is interpreted as a fold, while the brown dotted lines represent an interpreted Iron Rich Ultramafic Pegmatite (IRUP).

the structure of such thin mineralized reefs can be mapped indirectly using the seismic reflective interfaces between hanging wall and footwall rocks as proxies (Manzi *et al.*, 2020). For example, the MR is associated with the reflections arising from the contact between pegmatoidal anorthosite hanging wall and norite footwall. This implies that the MR is not imaged directly because of the low acoustic impedance contrast between the reef ($\rho = 2744$ kg/m³; $v = 5950$ m/s) and the surrounding rocks (norite: $\rho = 2951$ kg/m³; $v = 5667$ m/s; anorthosite: $\rho = 2947$ kg/m³; $v = 5530$ m/s). Due to weathering of the hanging wall, the MR is imaged indirectly due to the high acoustic impedance between the hanging wall (weathered anorthosite: $\rho = 2851$ kg/m³; $v = 3088$ m/s) and the footwall (norite: $\rho = 2951$ kg/m³; $v = 5667$ m/s). The UG2, on the other hand, is directly imaged because of the significant acoustic impedance contrast (mainly controlled by a high density associated with chromitite) between the UG2 ($\rho = 4392$ kg/m³; $v = 6118$ m/s) and the footwall ($\rho = 2700$ kg/m³; $v = 5900$ m/s) (R2 in Fig. 9).

The lateral extent of the geological feature cannot be discerned if it is narrower than the diameter of the first Fresnel zone (i.e., horizontal resolution limit) (Yilmaz *et al.*, 2001), which governs the horizontal positional accuracy of structural information that can be obtained from seismic data. It is worth noting that this horizontal resolution limit assumes that the seismic data are unmigrated. After migration, as is the case with our seismic data, this limit can be enhanced to approximately half the dominant wavelength, i.e. 21 m. Theoretically, this implies that two or more geological features within

21 m of each other will not be resolved as separate features. However, smaller features could still be detected, but this will depend on signal-to-noise ratio of the data, the velocity field and the migration algorithm used for migration (Manzi *et al.*, 2014; Westgate *et al.*, 2020).

A general assessment of the in-mine seismic results reveals that the data, although acquired in a noisy mine environment, are of high quality from which structural interpretation can be drawn. The strong, seismic reflections associated with the MR (~ 20–25 ms in Fig. 7a) and UG2 (~ 45–70 ms in Fig. 7a), although disrupted by faults and folds, are prominent and reliable indicators of mineralizations throughout the seismic profile (see, Figs 7, 8 and 9). The depth position, shape and dips of the interpreted MR and UG2 have been constrained with the geological information. Figure 10(a-d) shows the 3D visualization of the integrated borehole data, seismic data, mine modelled structures (MR, UG2, fault and dyke), seismically defined structures (faults and dykes). Generally, the seismic data has a good tie (within 3 m discrepancy) with the borehole information (Fig. 10a). For example, BH1 intersected the MR and UG2 at a depth of 68 m and 120 m below the tunnel respectively, which correspond to the depth position of reflections R1 and R2 on the migrated section (Fig. 10a). The seismic reflections R1 and R2 show a good correlation with the mine MR and UG2 orebodies, respectively (Fig. 10b). Surface boreholes (e.g., BH2) on the western side of the seismic line (Fig. 2b) intersected the MR at an average depth of 510 m and UG2 at an average depth of 555 m below surface, while the boreholes on the eastern side of the seismic profile
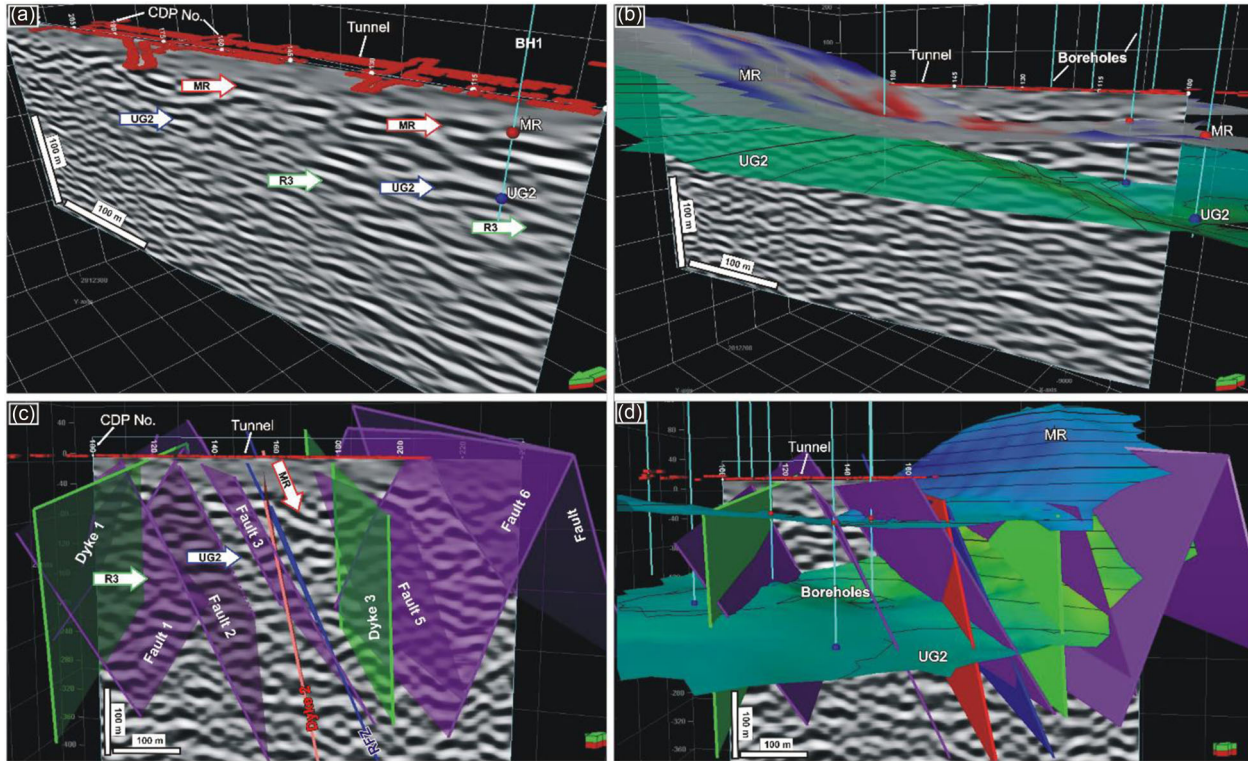
Figure 10 Depth-converted migrated seismic section plotted in 3D view together with the mine tunnel around 550 m below Earth's surface. (a) Correlation between the seismic section and borehole intersections of the MR (red) and UG2 (blue). (b) Correlation between the seismic reflections (R1 and R2) with MR (grey, red, and blue surface) and UG2 (green contoured surface) mine orebodies. (c) Seismic section together with interpreted and mine modelled faults and dykes overlaid. The Rapetsoa Fault Zone (RFZ) is shown in blue, crosscutting the mineralizations (MR, UG2 and R3). (d) Seismic section with boreholes, Merensky Reef (MR) and UG2 mine orebodies, structural interpretations (faults and dykes). The green arrow is pointing to the south.

intersected the MR and UG2 at 515 m and 570 m, respectively, indicating that these two target mineralizations are closer to each other on the western side (Fig. 10b). The boreholes were targeting the MR and UG2, thus did not extend to depths below UG2. Therefore, these boreholes were not used to constrain the source of R3 reflectivity in the seismic data. The minor discrepancies (0–3 m) in depth positions between seismics, orebodies and borehole data might be due to three reasons: (1) the boreholes were projected onto the seismic profile as they were not drilled directly along the seismic line, resulting in the interpreted reflection on the seismic profile having an apparent dip compared to the borehole data, therefore we expect a mismatch of the on a seismic line and the geological model (Fig. 4); (2) the velocity model used to depth convert the seismic sections may be in error; and (3) the mine orebody models are poorly constrained in areas that are not covered by the borehole information (western portion of the study area).

In terms of structural interpretation, our results confirm the existence of previously known faults and dykes (e.g.,

RFZ and dyke 2 in Figs. 4 and 10c) and further constrain their interpretation. F4 may represent one of the reactivated subordinate faults (e.g. RFZ) associated with the major Rustenburg fault, which has been studied by several authors (e.g., Scheiber-Enslin and Manzi, 2018; Basson, 2019) and confirmed through underground and surface mapping and drilling. Along the fault zone, we have also interpreted a dyke (D2) that corresponds to the one found in the mine model (Fig. 4). Therefore, our results suggest that the RFZ was active (or re-activated) and provided planes of weakness along which dyke 2 intruded. Furthermore, this work has identified more faults (e.g., f1–f7 in Figs 9 and 10c, d) and dykes (dyke 1 and dyke 3 in Fig. 10c, d) that were not incorporated in the existing mine geological model. The majority of the faults in the area are dipping at 60–90° WSW. The faults (Fig. 9; f1, f4, f5 and f7) are mainly reverse faults with a WSW upthrow, displacing the MR and UG2 horizons. F2 and f3 are normal faults dipping WSW, while f6 dips ENE (Fig. 10c).

In general, the geometry of R1 and R2 corresponds with the geometry of the mine MR and UG2 orebodies. Good correlation between seismics and mine orebodies is mainly observed from the centre (common depth point (CDP) no. 160) to the eastern end (CDP no. 100) of the profile (Fig. 10b, d). However, the seismic data suggest that these two horizons (R1 and R2) are faulted towards the far western end of the profile (CDP no. 160–240) with the downthrow in the west. This suggests that MR and UG2 are continuous on the western side of the outcrop position, which contradicts the geometry shown in the mine orebodies (Figs 2c and 10b). If our interpretation is correct, the continuity of these horizons beyond the outcrop position will need to be incorporated in the current mine model to enhance the resource evaluation. The seismic results suggest that faults and dykes crosscut and displace (in the case of faults) the MR, UG2 and R3 horizons, which constrains their timing of activity (i.e., they were active after the reefs depositions). The delineation of these structures is important for future mine planning at Maseve mine as these indicate areas that may not be mineable because of the loss of ground. Although these faults are detected on the seismic section, their throws cannot be determined with confidence as their displacements (throws) are below the seismic resolution limit of the data. In addition to this, the seismic data provide information on a potential chromitite-rich horizon (reflection R3 in Fig. 9) tens of metres in the footwall of the UG2 horizon, which is interpreted as the UG1.

In the future, we plan to overlap (at least by 50% of each profile length) the profiles to avoid obtaining low folds at the end of each profile. In the new data, other processing approaches (such as pre-stack depth and diffraction imaging) will be tested to further improve the imaging of the structures in this area and further investigate the sources of other reflections (including R3). While a longer single profile would have provided better results and allowed deeper imaging, the study was constrained by the available recording system we have (48 channel recording system) and the limited budget to hire a suitable seismic system. In addition to this study, other seismic profiles are being processed and the results will be integrated with the GPR data collected along the same profiles to constrain the geological interpretation.

Given the cost-effective nature of the instruments used and the limitation posed by mine infrastructure to properly design in-mine seismic surveys, the results demonstrate that in-mine seismic surveys can be an asset for mineral exploration and mining. Furthermore, these experimental surveys are considered to be cost-effective as the approach was approximately > 60% cheaper than if the survey was acquired by commercial contractors on surface (assuming that there would be no infrastructure limitations, environmental and permitting issues) using more expensive and heavier geophysical equipment (such as vibroseis trucks and 100s of receivers on surface).

CONCLUSIONS

In-mine seismic experiments were conducted at Maseve mine to image the host rocks, geological structures and the platinum deposits. The surveys involved careful planning through mine visits and using mine geological models and borehole data. This project is a joint effort between South African academic, research, government and mining institutions. While the results of the experiments are encouraging considering they were conducted inside underground mine tunnels in a structurally complex hard rock mining environment, the survey designs and processing of the data were challenging due to flooded mining tunnels causing issues with land streamer sensor-ground coupling; the hard rock environment making it difficult to plant geophones (cabled); loose tunnel hanging wall limiting the use of a heavier energy sources; and fractured tunnel walls and mine infrastructure producing complicated wavefield characteristics (e.g., tunnel guided waves) that are difficult to handle in a 2D scenario.

We demonstrate that the seismic method can be used inside mine tunnels to delineate geological features associated with mineral deposits and improve mining. The processing of the in-mine seismic data provided insight into the location of the Merensky Reef (MR) and Upper Group-2 (UG2) below the mine tunnel, and an additional potential resource below UG2. Despite the challenges faced in the design and processing of the data, the target MR and UG2 orebodies have been imaged with confidence, supported by the geological model. Synthetic data constrained our seismic interpretations, although the model can be improved with more borehole data to constrain the targeted mineralizations. The reported data are only a portion of the full dataset, not including seismic and GPR profiles that are nearly perpendicular to the reported merged profiles. Exploitation of the full dataset will enable the characterization of both the MR and the UG2 in detail. The study forms a pilot concept for the mining industry to utilize in-mine seismics development and mine planning. This survey set-up is cost-effective because it uses an affordable energy source and land streamer, which do not require extensive planning and mobilization.

ACKNOWLEDGEMENTS

DATA AVAILABILITY STATEMENT

Seismic and borehole research data that support the findings of this study are available on request from the corresponding author. The data are not publicly available due to privacy restrictions. Geological outcrop and open-source borehole data can be found on the website of The Council for Geoscience South Africa (https://maps.geoscience. org.za/portal/apps/sites/?fromEdit=true#/interactivewebmap).

ORCID

Moyagabo K. Rapetsoa
https://orcid.org/0000-0003-3275-8994
Musa S.D. Manzi https://orcid.org/0000-0002-1654-5211
Mpofana Sihoyiya
https://orcid.org/0000-0003-1956-5223
Ian James https://orcid.org/0000-0002-1655-3529

REFERENCES

Ahmadi, O., Koyi, H., Juhlin, C. and Gessner, K. (2016) Seismic signatures of complex geological structures in the Cue-Weld Range area, Murchison domain, Yilgarn Craton, Western Australia. *Tectonophysics*, 689, 56–66. https://doi.org/10.1016/j.tecto.2016.02.020

Basson, I.J. (2019) Cumulative deformation and original geometry of the Bushveld complex. *Tectonophysics*, 750, 177–202. https://doi.org/10.1016/j.tecto.2018.11.004

Brodic, B., Malehmir, A. and Juhlin, C. (2017) Delineating fracture zones using surface-tunnel-surface seismic data, P-S, and S-P mode conversions. *Journal of Geophysical Research: Solid Earth*, 122(7), 5493–5516. https://doi.org/10.1002/2017JB014304

Brodic, B., Malehmir, A., Pacheco, N.B.M., Juhlin, C., Carvalho, J., Dynesius, L., et al. (2021) Innovative seismic imaging of VMS deposits, Neves-Corvo, Portugal: Part I - In-mine array. *Geophysics*, 1–76. https://doi.org/10.1190/geo2020-0565.1

Buchanan, P.C. and Reimold, W.U. (1998) Studies of the Rooiberg group, Bushveld complex, South Africa: no evidence for an impact origin. *Earth and Planetary Science Letters*, 155(3–4), 149–165. https://doi.org/10.1016/S0012-821X(97)00216-1

Campbell, G. (2011) Exploration geophysics of the Bushveld complex in South Africa. *The Leading Edge*, 30(6), 622–638. https://doi.org/10.1190/1.3599148

Cawthorn, R.G. (2015) The Bushveld complex, South Africa. In: Charlier, B., Namur, O., Latypov, R. & Tegner, C. (Eds.) *Layered intrusions*. Dordrecht: Springer Netherlands, pp. 517–587. https://doi.org/10.1007/978-94-017-9652-1_12

Cawthorn, R.G. and Webb, S.J. (2001) Connectivity between the western and eastern limbs of the Bushveld complex. *Tectonophysics*, 330(3–4), 195–209. https://doi.org/10.1016/S0040-1951(00)00227-4

Chistyakova, S., Latypov, R. and Youlton, K. (2019) Multiple Merensky reef of the Bushveld complex, South Africa. *Contributions to Mineralogy and Petrology*, 174(3), 26. https://doi.org/10.1007/s00410-019-1562-x

Donoso, G.A., Malehmir, A., Brodic, B., Pacheco, N., Carvalho, J. and Araujo, V. (2021) Innovative seismic imaging of VMS deposits, Neves-Corvo, Portugal: Part II. Surface array. *Geophysics*, 1–39. https://doi.org/10.1190/geo2020-0336.1

Eales, H.V. and Cawthorn, R.G. (1996) The Bushveld complex. In *Developments in petrology* (Vol. 15). Elsevier, pp. 181–229. https://doi.org/10.1016/S0167-2894(96)80008-X

Guo, J. and Luo, C. (2014) Application of tunnel seismic image approach to the advanced geological prediction for tunnel. *Journal of Multimedia*, 9(7), 879–886. https://doi.org/10.4304/jmm.9.7.879-886

Hunt, E., Latypov, R. and Horváth, P. (2018) The Merensky cyclic unit, Bushveld complex, South Africa: reality or myth? *Minerals*, 8(4), 144. https://doi.org/10.3390/min8040144

Kgarume, T.E., Van Schoor, A.M. and Nontso, Z. (2019) The use of 3D ground-penetrating radar to mitigate the risk associated with falls of ground in Bushveld Complex platinum mines. *The Journal of the Southern African Institute of Mining and Metallurgy*, 119, 973–982.

Kinnaird, J.A. (2005) *The Bushveld Large Igneous Province, Review Paper*. University of the Witwatersrand, Johannesburg, 39 pp. http://www.largeigneousprovinces.org/sites/default/files/BushveldLIP.pdf [Accessed 11th November 2021].

Ledwaba, L.S., Scheepers, J., and Durrheim, R.J. (2012) Rockburst damage mechanism at impala platinum mine: The Southern African Institute of Mining and Metallurgy, pp. 20.

Lee, C.A. (1996) A review of mineralization in the Bushveld complex and some other layered intrusions. *Developments in Petrology*, 15, 103–145. https://doi.org/10.1016/S0167-2894(96)80006-6

Malehmir, A., Durrheim, R., Bellefleur, G., Urosevic, M., Juhlin, C., White, D.J. et al. (2012) Seismic methods in mineral exploration and mine planning: a general overview of past and present case histories and a look into the future. *Geophysics*, 77(5), WC173–WC190. https://doi.org/10.1190/geo2012-0028.1

Malehmir, A., Andersson, M., Lebedev, M., Urosevic, M. and Mikhaltsevitch, V. (2013) Experimental estimation of velocities and anisotropy of a series of Swedish crystalline rocks and ores: velocities and anisotropy of a series of crystalline rocks and ores. *Geophysical Prospecting*, 61(1), 153–167. https://doi.org/10.1111/j.1365-2478.2012.01063.x

Malehmir, A., Bergman B., Andersson B., Sturk R. and Johansson, M. (2018) Seismic imaging of dyke swarms within the Sorgenfrei–Tornquist Zone (Sweden) and implications for thermal energy storage. *Solid Earth*, 9, 1469–1485.

Manzi, M., Durrheim, R. and Webb, S. (2017) 3D seismic attributes for platinum exploration and mine planning in the Bushveld complex (South Africa). In *International Geophysical Conference, Qingdao, China, 17–20 April 2017* (pp. 665–668). Qingdao, China: Society of Exploration Geophysicists and Chinese Petroleum Society. https://doi.org/10.1190/IGC2017-169

Manzi, M., Malehmir, A. and Durrheim, R. (2019) The value of seismics in mineral exploration and mine safety. In *81st EAGE Conference and Exhibition 2019* (pp. 1–5). London, UK: European Association of Geoscientists & Engineers. https://doi.org/10.3997/2214-4609.201901667

Manzi, M.S.D., Cooper, G.R.J., Malehmir, A. and Durrheim, R.J. (2020) Improved structural interpretation of legacy 3D seismic data from Karee platinum mine (South Africa) through the application of novel seismic attributes. *Geophysical Prospecting*, 68(1), 145–163. https://doi.org/10.1111/1365-2478.12900

Manzi, M.S.D., Durrheim, R.J., Hein, K.A.A. and King, N. (2012) 3D edge detection seismic attributes used to map potential conduits for water and methane in deep gold mines in the Witwatersrand basin, South Africa. *Geophysics*, 77(5), WC133–WC147. https://doi.org/10.1190/geo2012-0135.1

Manzi, M.S.D., Hein K.A.A., Durrheim R.J. and King N., (2014), The Ventersdorp contact reef model in the Kloof gold mine as derived from 3D seismics, geological mapping and exploration borehole datasets. *International Journal of Rock Mechanics and Mining Sciences*, 66, 97–113.

Muller, C.J. and Visser (2010) Resource cut estimation of the western Bushveld joint venture (WBJV) located on the western limb of the Bushveld igneous complex, 7. http://s1.q4cdn.com/169714374/files/doc_downloads/Technical-Report-WBJV-Project-3-10-08-31-filed-10-10-05-Certificate.pdf

Nex, P.A., Ingle, L.J., Kinnaird, J.A., van der Vyver, B.A. and Cawthorn, R.G. (1998) A new stratigraphy for the main zone of the Bushveld complex, in the Rustenburg area. *South African Journal of Geology*, 101(3), 215–223.

Nkosi, N.Z., Manzi, M.S.D., Drennan, G.R. and Yilmaz, H. (2017) Experimental measurements of seismic velocities on core samples and their dependence on mineralogy and stress, Witwatersrand Basin (South Africa). *Studia Geophysica et Geodaetica*, 61(1), 115–144. https://doi.org/10.1007/s11200-016-0804-x

Scheiber-Enslin, S.E. and Manzi, M. (2018) Integration of 3D reflection seismics and magnetic data for deep platinum mine planning and risk mitigation: a case study from Bushveld Complex, South Africa. *Exploration Geophysics*, 49(6), 928–939. https://doi.org/10.1071/EG17083

Seabrook, C.L. (2005) *The upper critical and lower main zones of the eastern Bushveld complex*. PhD thesis, University of the Witwatersrand, Johannesburg, South Africa. p284.

Sehoole, L., Manzi, M.S.D., Zhang, S.E. and Bourdeau, J.E. (2020) An innovative seismic and statistical approach to understand 3D magmatic structures and ore deposits in the western Bushveld Complex, South Africa. *Ore Geology Reviews*, 126, 103784. https://doi.org/10.1016/j.oregeorev.2020.103784

Singh, B., Górszczyk, A., Malehmir, A., Hlousek, F., Buske, S., Sito, Ł. and Marsden, P. (2020) 3D velocity model building in hardrock environment using FWI: a case study from Blötberget Mine, Sweden. In *NSG2020 3rd Conference on Geophysics for Mineral Exploration and Mining* (pp. 1–5). : European Association of Geoscientists & Engineers. https://doi.org/10.3997/2214-4609.202020122

Stevenson, F. and Durrheim, R.J. (1997) Reflection seismics for gold, platinum and base metal exploration and mining in southern Africa. In: Gubins, G. (Ed.) *Proceedings of Exploration 97: 4th Decennial International Conference on Mineral Exploration*, pp. 391–398.

Stevenson, F., Higgs, R.M.A. and Durrheim, R.J. (2003) Seismic imaging of precious and base metal deposits in southern Africa, Chapter 9. In: Eaton, D., Salisbury, M., and Milkereit, B (Eds.) *Hardrock seismic exploration*. Houston, TX: Developments in Geophysics Series, Society of Exploration Geophysicists, pp. 141–156.

Trickett, J.C., Duweke, W.A. and Kock, S. (2004) Three-dimensional reflection seismics: worth its weight in platinum. *Journal of the South African Institute of Mining and Metallurgy*, 105, 257–263.

Webb, S.J., Cawthorn, R.G., Nguuri, T. and James, D. (2004) Gravity modeling of Bushveld complex connectivity supported by Southern African seismic experiment results. *South African Journal of Geology*, 107(1–2), 207–218. https://doi.org/10.2113/107.1-2.207

Westgate, M., Manzi, M.S.D., James, I. and Harrison, W. (2020) New insights from legacy seismic data: reprocessing of legacy 2D seismic data for imaging of iron-oxide mineralization near Sishen Mine, South Africa. *Geophysical Prospecting*, 68(7), 2119–2140. https://doi.org/10.1111/1365-2478.12996

Yilmaz, O., Yilmaz, Ö. and Doherty, S.M. (2001) Seismic data analysis: processing, inversion, and interpretation of seismic data. *Society of Exploration Geophysicists*. Retrieved from https://books.google.co.za/books?id=ceu1x3JqYGUC